



Hydrogen solubility in Zr–Nb alloys

Vidur Tuli^a, Antoine Claisse^b, Patrick A. Burr^{a,*}

^a School of Mechanical and Manufacturing Engineering, University of New South Wales, Australia

^b Westinghouse Electric Sweden, AB, Västerås 721 63, Sweden

ARTICLE INFO

Keywords:

Hydrogen trapping
Hydrogen embrittlement
Radiation effects
Zirconium alloys
DFT

ABSTRACT

We present a fast and accurate method for predicting the thermodynamics of hydrogen solubility and trapping in alloys, which is two orders of magnitude faster than conventional ab-initio approaches. The model hinges on the finding that the solubility of H is dominated by its nearest neighbour environment. We apply the method to the problem of hydrogen redistribution in Nb-containing Zr nuclear fuel cladding, and validated it against brute-force ab-initio approaches. We find that hydrogen preferentially dissolves into the β -Zr phase found in as-manufactured 2.5%Nb alloys, and H is likely to redistribute into the α phase following the irradiation-induced decomposition of β -Zr. β -Nb particles found in as-manufactured 1%Nb alloys may act as weak sinks for H, however irradiation-induced change of composition of β -Nb particles increases their hydrogen-trapping strength. Nano-platelets formed under irradiation in these alloys are potentially even stronger hydrogen sinks, especially if induced by proton irradiation rather than neutrons.

Hydrogen embrittlement is a long-standing issue for many advanced alloy systems [1–6]. Hydrogen enters virtually all alloys, and then redistributes through the microstructure in ways that can be detrimental to the mechanical performance of the alloy. A key obstacle in addressing hydrogen embrittlement is the difficulty in locating hydrogen experimentally, meaning that most advances are the result of inferred observations [7–9].

An exemplar case of hydrogen-induced degradation is found in the nuclear industry, where hydrogen enters the nuclear fuel cladding (Zr alloys) from the core coolant, and may cause dimensional changes, embrittlement, and delayed hydride cracking, limiting the useful life of nuclear fuel in the reactor [1–3,10,11]. Nb is often used as an alloying addition to improve the oxidation kinetics [12–16] and reduce the hydrogen pick-up of Zr alloys [17–20]. Nb is soluble in the α phase to 0.6 at.% Nb at the monotectoid temperature of 620 °C [21], and above that it precipitates as either β -Nb (75–90 wt.% Nb) [22–25] or metastable β -Zr (20–50 wt.% Nb) [26,27], depending on processing conditions. The presence, composition and volume fraction of Nb-containing phases is known to affect hydrogen thermodynamics. In particular, increasing the content of β -Zr leads to an increase in H terminal solid solubility (TSS) [28,29], which is not observed with increasing β -Nb volume fraction [29,30].

The issue is rendered more complex by the fact that the composition and morphology of these phases changes while in service. Under neutron

irradiation β -Zr decomposes into α -Zr and β -Nb, while primary β -Nb particles may dissolve and/or reduce the Nb content to as low as 55 wt.% [24,25,31,32]. The formation of irradiation-induced platelet-like precipitates have also been reported in these alloys, with composition of ~60 wt.% Nb under neutron flux [25,33], 10–40 wt.% Nb under proton irradiation [34].

The irradiation-induced evolution of the microstructure is likely to cause hydrogen redistribution, but we lack a mechanistic understanding of how hydrogen interacts with these phases as they change over time. In particular, there is limited knowledge of the relative solubility and trapping strength of hydrogen in these phases [11,35–37]. Here we shed light on the thermodynamic drive for trapping and dissolution using two ab-initio methods. First we use a conventional approach that relies on large statistical sampling of the various local environments in which hydrogen may reside within these solid solutions. Then, exploiting the finding that the solution energy is strongly linked to the nearest neighbour composition, we develop a highly-scalable method for predicting hydrogen solubility in arbitrary binary compositions.

In the first method, we describe the disorder of a BCC-(Zr,Nb) solid solution using special quasi-random structures (SQS), generated using the MCSQS code [38] with pair, triplet and quadruplet correlations defined up to the third, second and first nearest neighbour, respectively. We use 128-atom supercells with 25 at.% Nb and 75 at.% Nb to represent β -Zr and β -Nb, respectively. These structures were fully relaxed

* Corresponding author.

E-mail address: p.burr@unsw.edu.au (P.A. Burr).

<https://doi.org/10.1016/j.scriptamat.2022.114652>

Received 13 October 2021; Received in revised form 21 January 2022; Accepted 3 March 2022

Available online 19 March 2022

1359-6462/© 2022 Acta Materialia Inc. Published by Elsevier Ltd. All rights reserved.

using density functional theory (DFT) simulations carried out using the VASP code [39,40] with the PBE functional, an plane-wave cut-off of 350 eV, a $3 \times 3 \times 3$ k -point grid and Methfessel–Paxton band smearing 0.1 eV. The lattice parameters of all phases are in excellent agreement with experimental literature, see Table 1.

In a solid solution, H may be accommodated in a wide range of different environments, each with its own energy. The distribution of solution energies was calculated by placing a single hydrogen atom in 100 randomly-selected and symmetrically unique sites per composition, and further relaxing the atomic positions (lattice vectors kept constant). These are referred to as explicit calculations henceforth. The relative change in solution energy for an interstitial site i , compared to α -Zr, is calculated as

$$\Delta E_{sol,i}^H = \left(E_{\alpha\text{-Zr}}^{DFT} + E_{\beta+\text{H},i}^{DFT} \right) - \left(E_{\alpha\text{-Zr}+\text{H}}^{DFT} + E_{\beta}^{DFT} \right) \quad (1)$$

where $E_{\alpha\text{-Zr}}^{DFT}$ and E_{β}^{DFT} represent the DFT energy of perfect supercells of α -Zr and β -(Zr,Nb), respectively. A subscript $+\text{H}$ implies the addition of an interstitial H atom.

The probability of filling each of those sites ($P_i(E, T)$) follows Maxwell–Boltzmann statistics

$$P_i(T) = \frac{e^{-E_i/k_B T}}{\sum_i e^{-E_i/k_B T}} \quad (2)$$

thus, the expectation value of the solution energy, $\langle \Delta E_{sol}^H(T) \rangle$, at a finite temperature T is

$$\langle \Delta E_{sol}^H(T) \rangle = \sum_i E_{sol,i} P_i(T) \quad (3)$$

with a standard deviation

$$\sigma = \sqrt{\langle \Delta E_{sol}^H(T)^2 \rangle - \langle \Delta E_{sol}^H(T) \rangle^2} \quad (4)$$

where

$$\langle \Delta E_{sol}^H(T)^2 \rangle = \sum_i E_{sol,i}^2 P_i(T) \quad (5)$$

Looking at unary systems first, we find that ΔE_{sol}^H is strongly exothermic for BCC-Zr (-0.28 eV), while the energy difference is negligible for BCC-Nb (0.02 eV). This is consistent with available literature, which suggests that H is more soluble in BCC-Zr compared to HCP-Zr, whereas the difference in H solubility between HCP-Zr and BCC-Nb is negligible [29,44].

Moving to the binary β solid solution, Fig. 1a shows the distribution of ΔE_{sol}^H at the 2 different compositions considered. The results make it clear that the solubility of H in BCC-(Zr,Nb) increases with increasing Zr content, and $\Delta E_{sol,i}^H$ of most sites falls between the end members' minimum $\Delta E_{sol,i}^H$ (vertical lines). Fig. 1b shows the resulting $\langle \Delta E_{sol}^H(T) \rangle$, obtained from thermodynamic averaging at 0–900 K. This suggests that H is more soluble in β -Zr compared to β -Nb at all temperatures. These results are supported by experimental observations that the TSS increases with increasing β -Zr phase fraction [28,29].

Fig. 1 b also shows that below ~ 72 K, addition of 25 at.% Nb leads to

a reduction of the H solution energy to below that of pure BCC-Zr. This is attributed to the dual effect of introducing a solute into BCC-Zr: on the one hand Nb additions monotonically affect global properties of the solution from those of BCC-Zr to those of BCC-Nb (e.g. lattice parameter, which follows Vegard's law, average electron density, elastic constants); this is expected to increase ΔE_{sol}^H smoothly from -0.28 eV (of BCC-Zr) to 0.02 eV (of BCC-Nb). On the other hand, Nb additions also create discrete local environments in which H may be accommodated, which results in a broadening of the ΔE_{sol}^H . At low concentrations, the broadening effect may be greater than the linear change in global properties, resulting in few states with energy lower than the end member. These states have a greater occupancy at lower temperatures. While this is of little consequence in the case of 25 at.% Nb, as the temperature at which the cross-over happens is below room temperature, it is possible that smaller additions of Nb may lead to a stronger reduction than that observed in the case of 25 at.% Nb. Interestingly, we have found that H consistently relaxed into tetrahedral sites, irrespective of its starting position. This is consistent with H behaviour in other BCC systems [44–48].

Fig. 2 a shows the relationship between ΔE_{sol}^H and the number of Zr atoms in H's nearest neighbour (NN) shell. ΔE_{sol}^H decreases consistently with increasing number of neighbouring Zr atoms, suggesting that the local composition is a key driver in H solution energy. Fig. 2b shows similar results for H solubility in $\text{Zr}(\text{Fe,Cr})_2$, reproduced from data published by Jones *et al.* [48], showing a similar trend, but limited to a maximum number of two Zr NN due to the crystallography of $\text{Zr}(\text{Fe,Cr})_2$. More detail on the strongly-local binding of H in β -(Zr,Nb) is provided in the supplementary material.

Similar trends of localised hydrogen interactions have been reported in a range of materials. Local binding environment are thought to drive H trapping in carbides over BCC-Fe [49]. In Fe-Cr solutions H prefers sites with higher Cr content [50], in AB_2 laves phases ($A = \text{Zr, Ti}$; $B = \text{Ni, Mn, Cr, V}$) sites with 2 Zr NN atoms [51,52], and in Ti–Zr–Ni alloys, sites surrounded by Ti and Zr neighbours [53]. Attraction of H to transition metals is reported to reduce with increasing electrons in the d-band [54]. This might explain H's preference for more Zr neighbours over Nb.

Based on the observations that NN composition dominates the solution energy of H in Zr-Nb solid solutions, we have created a model to predict the solubility of H at any composition of BCC-(Zr,Nb) from few DFT calculations. We define each accommodation site as a discrete state i , with energy E_i , and associated density of sites D_i . We then split E_i into two terms

$$E_i(x) = E_i^0(N, n) + \Delta E_i \quad (6)$$

where E_i^0 represents the energy contribution from the local environment containing N atoms of which n are of type B (here Nb), and ΔE_i represents the energy contribution from all other (possibly unknown) global effects of the solid solution (e.g., average changes to the lattice parameters, elastic constants, charge density, etc.).

The term E_i^0 is calculated through a set of DFT simulations in which a H atom is surrounded by a cluster of n B atoms embedded in a supercell of A atoms (E_A) and again the same cluster embedded in a supercell of B atoms (E_B). The energy of hydrogen solution in these clusters is shown in Fig. 3a. ΔE_i is approximated with a mean field approach that describes a continuous linear energy contribution bounded by the two end-members E_A and E_B , so that

$$E_i(n, x) = \Omega_i E_A(n) + x \Omega_i (E_B(n) - E_A(n)) \quad (7)$$

where Ω_i is the multiplicity of state i , defined as the number of symmetrically equivalent states divided by the total number of states of the same composition n/N .

With this approximation, the distribution of energies is bound by that of the end members, i.e. $E_{(x=0)} = E_A$ and $E_{(x=1)} = E_B$. N may be treated as a convergence parameter, separating the region where the mean field

Table 1

Lattice parameters from DFT relaxation of special quasi-random structures, and literature values.

Element	Lattice parameters (\AA)	
	Current work	Literature
BCC-Zr	3.56	3.59 [41], 3.57 [42]
β -Zr	3.48	3.49 [42]
β -Nb	3.36	3.36 [42]
BCC-Nb	3.30	3.29 [43], 3.31 [42]

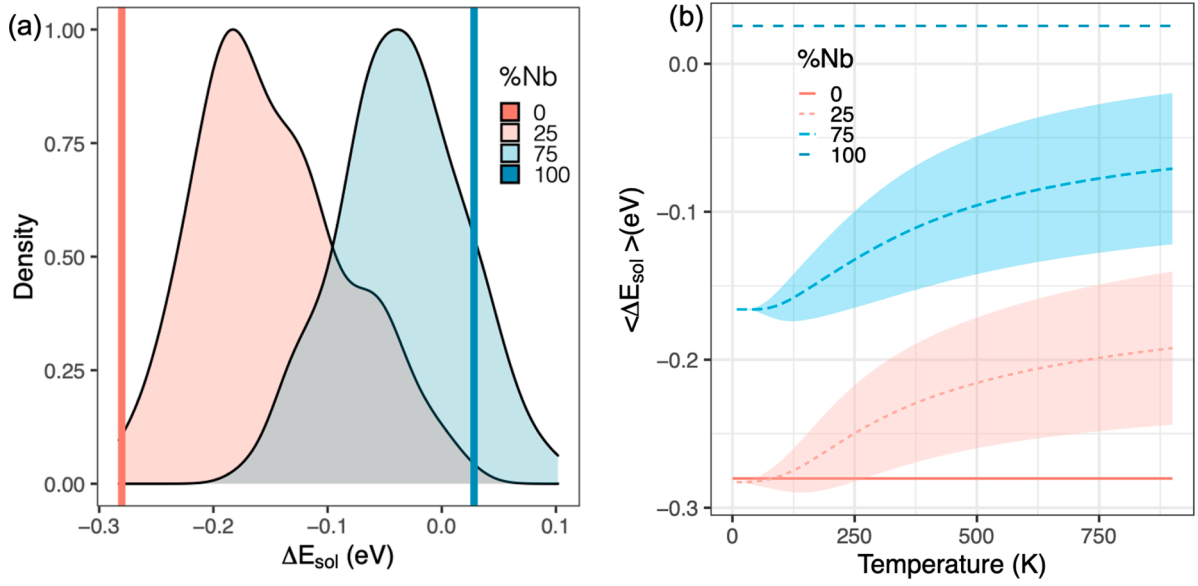


Fig. 1. (a) ΔE_{sol}^H in β -Zr and β -Nb phases obtained through 100 DFT calculations at each composition, and (b) the expected solution energy at different averaging temperature (line) with one standard deviation (shading).

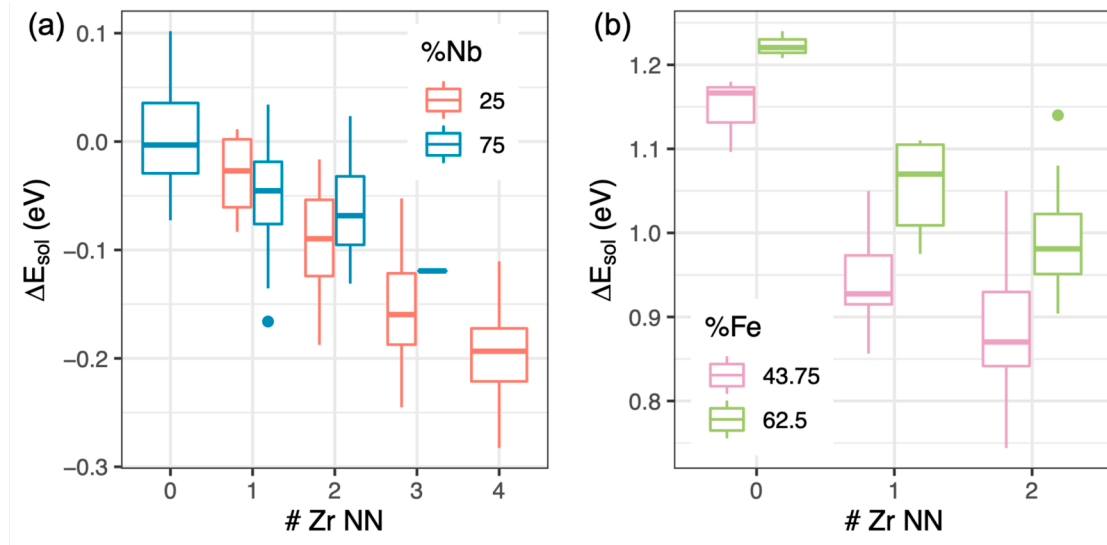


Fig. 2. Box and whiskers plot of ΔE_{sol}^H as a function of number of Zr atoms in 1st NN shell in (a) BCC-(Zr,Nb) and (b) Zr(Fe,Cr)₂. The bar represents the median ΔE_{sol}^H and the width of the box represents the Q1–Q3 interquartile range. The whiskers represent the 95% confidence interval and the dots represent outliers.

approach is valid from the region where the discrete states must be accounted for explicitly. In this work we use $N = 4$, as the strength of interactions decreases markedly past the first nearest neighbour shell (which contains 4 atoms, in this case). Note that we may have multiple E_i values for a given set of n , N and x , since two or more symmetrically non-equivalent clusters i may exist with the same composition n/N .

Within the bounds set by E_A and E_B , $D(E)$ describes the density of states with energy E_i . Since E_i is a unique function of the state i , $D(E)$ can be defined as the relative density, D_i , of state i in an alloy of composition x . In other words, D_i is the probability of finding a region of space containing N atoms of composition n/N . In an ideal solid solution, this distribution is accurately described by a binomial distribution:

$$D_i = \frac{N!}{(N-n)!n!} x^n (1-x)^{N-n} \quad (8)$$

The expectation value of the solution energy at a finite temperature T

is then evaluated using Eq. (3), with modified $P_i(T)$:

$$P_i(T) = \frac{D_i e^{-E_i/k_B T}}{\sum_i D_i e^{-E_i/k_B T}} \quad (9)$$

The input DFT data for the model, ΔE_{sol}^H of H in surrounded by clusters of varying composition, is shown in Fig. 3a. We again observe the 1st NN chemistry affecting the H solubility more than the difference between the two materials in which the cluster is embedded in. The two points at $n = 2$ are due to the symmetrically different configurations in which two atoms of a tetrahedral site may be arranged in a BCC crystal. The results of the model, D_i (y-axis) and E_i (x-axis), are shown in Fig. 3b for ten compositions, showing the progressive change in solution energy as a function of Nb content. Only five individual states make up each density distribution, which are joined using locally weighted smoothing.

Fig. 3 c and d compares the output of the model to the explicit calculations. The peaks in both cases represent the highest value of D_i ,

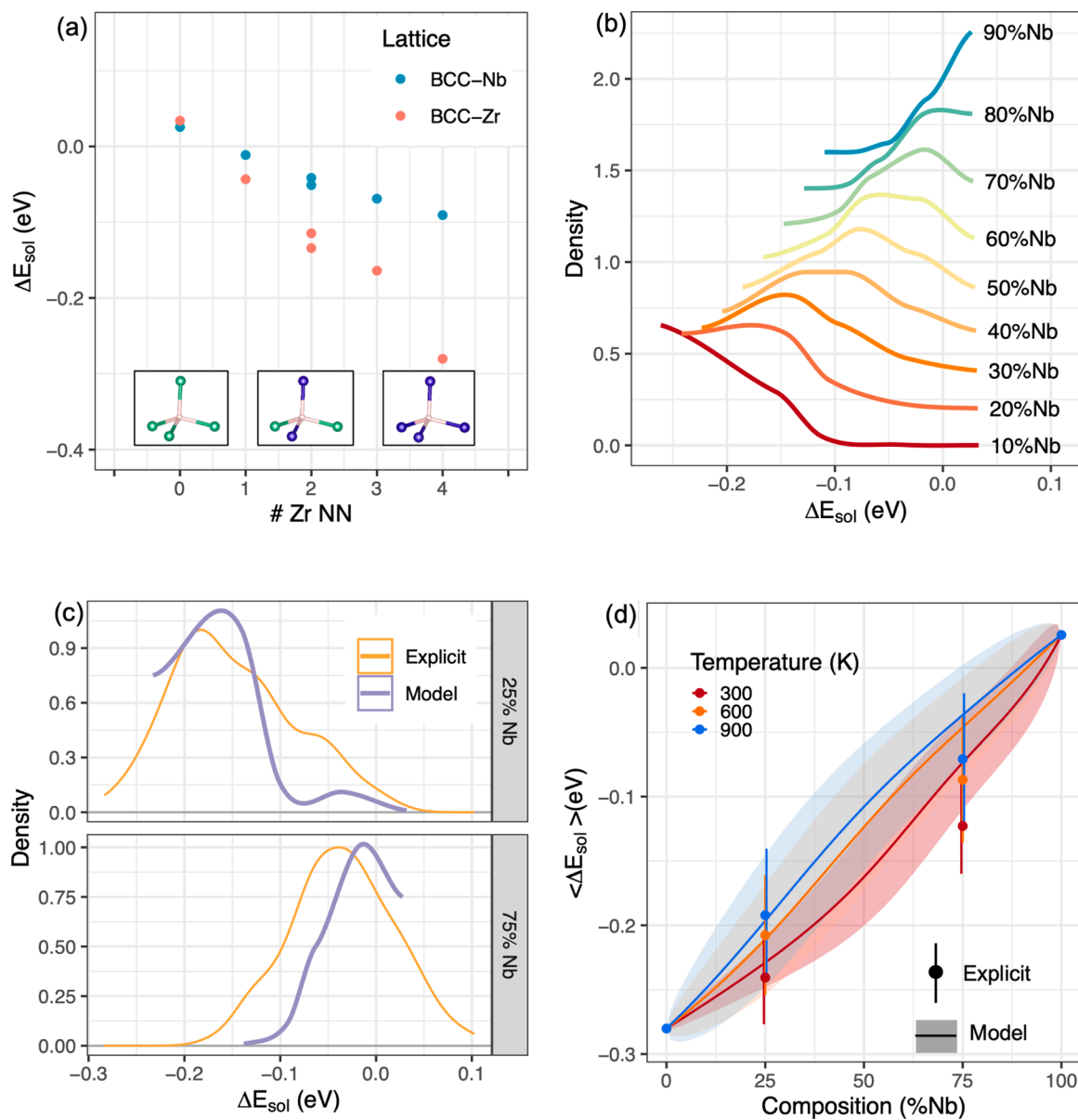


Fig. 3. (a) input values for the model: H solution energy in clusters in BCC-Zr and BCC-Nb. (b) model output for multiple compositions, vertically offset by increments of 0.2 density to aid clarity of presented results. (c) model D(E) vs. explicit calculations for two compositions. (d) model $\langle \Delta E_{sol}^H(T) \rangle$ vs. explicit calculations at three averaging temperatures, where shaded area and bars represent one standard deviation.

which correspond to sites with 3 and 1 Zr NN for 25 at.% Nb and 75 at.% Nb, respectively. A limitation of the model is that the prediction of the energy distribution cannot be extrapolated beyond the energy of the end members of the cluster simulations of Fig. 3a that inform it, and thus appears truncated. Nevertheless, the model correctly predicts that H is more soluble in β -Zr than β -Nb, and captures the correct range of energies. Additionally, the model correctly predicts the general shape of the distribution and the effect of change in composition, albeit with a systemic shift towards higher energies of ~ 0.02 eV in the peak energy density. Such slight shift could be due to the lattice expansion by the addition of H, which is known to be small [55], and which may be different in the disordered SQS structures (explicit calculations) compared to the pure end-members (predictive model). Similarly, local changes in strain field and local electron density distribution, which are expected to be present in a disordered solid solution, are not explicitly modelled in the new approach, and are instead collectively treated as second-order effects approximated by the mean field approach.

It must be stressed that the model was informed by 12 DFT simula-

tions, while each of the explicit distribution was computed from 101 (computationally more intensive) DFT simulations, and the creation of a special-quasi random structure via a Monte Carlo algorithm. In all, the computational saving of the model is $\sim 96\%$ per composition (or 99.8% for both compositions of Fig. 3c). Overall, the agreement between the model predictions and explicit calculations is remarkable considering the computational savings achieved.

One key advantage of the model is that it can be used to predict the solubility at any composition of BCC-(Zr,Nb) at no additional cost (i.e., using the same 12 results of Fig. 3a). Neutron irradiation in 1% Nb, Zirlo, E110 and similar alloys leads to reduction of Nb content in β -Nb particles [24,25,56]. Our model predicts this depletion of Nb would increase the H trapping strength of β -Nb (Fig. 3b). In fact, in as manufactured alloys, very little H is expected to be dissolved in the β -Nb, as it has similar E_{sol} to α -Zr, but following dissolution the β -Nb particles might become sinks for H, unless stronger sinks have also developed in the microstructure.

Irradiation-induced formation of nano-sized β platelets have also

been reported to form concurrently to the dissolution of primary β -Nb particles in neutron-irradiated samples [25,33,34]. These are reported to have similar composition to the primary β -Nb particles, and therefore should have similar chemical binding to hydrogen, but additionally, their coherent or semi-coherent interfaces [34,57,58] may lead to significant strain fields, which may dominate the hydrogen trapping behaviour [59]. On the other hand, nanosized precipitate formed by proton irradiation exhibit a significantly lower Nb content compared to the neutron irradiated counterparts [34], which may lead to a markedly stronger trapping of H. Thus, particular care must be taken when using proton-irradiated samples as analogues of neutron-irradiated material to study the redistribution of H.

In the case of Zr-2.5%Nb and other alloys containing the metastable β -Zr, the model predicts that the majority of the hydrogen picked up will be trapped in the β -Zr phase, until it decomposes into α -Zr and β -Nb. After decomposition, hydrogen is likely to move out of the remaining β -Nb particles and redistribute towards nearby sinks, which are most likely microstructural defects within the α -Zr phase (dislocations, loops and grain boundaries) and hydrides.

Beyond the change in composition of the β phases, radiation damage also leads to a range of microstructural changes that are not explicitly modelled in our predictions [60]. In particular, the concentration of vacancy and dislocation loops, which are strong sinks for H [61–63], is known to increase in α -Zr. We expect similar defect to form in the β phases as well. However, there is limited knowledge on the concentration and H-trapping strength of these defects in the β phases, thus it is difficult to judge whether radiation-induced defects increase or decrease the H-trapping strength of β phases compared to defective α -Zr. Future improvements to the model could explore this by modelling vacancies in the input DFT cluster calculations.

In summary, using DFT calculations we show that the H solution energy is dominated by the nearest neighbour chemistry and configuration, both in β -(Zr,Nb) and other solid solutions. By decoupling these strongly local interactions from other (global) effects of the solid solution, we have developed a cost-effective method that accurately predicts the solution energy of hydrogen from few DFT simulations. With this method we show that the H solubility in β -(Zr,Nb) increases with increasing Zr content, leading to a considerably higher solubility of H in the β -Zr phase compared to the β -Nb phase. However, the compositional changes caused by neutron irradiation are likely to increase the solubility and trapping strength of Nb-depleted β -Nb particles, and radiation-induced β -Nb nano-sized platelets. For alloys containing the metastable β -Zr phase, at first H will preferentially dissolve into β -Zr, and then distribute out into the α -Zr matrix (likely at dislocation loops and other defects) as the metastable phase decomposes with increasing neutron fluence. The example above showcases the potential of the new method, which yields remarkably accurate results for a computational savings of two orders of magnitude (or more, depending on how many compositions need to be studied). This model may be applicable, with no modifications, to other binary systems, and with further testing to ternary or chemically complex alloys, opening the door to high-throughput screening of hydrogen trapping site in alloys that suffer from hydrogen embrittlement.

Declaration of Competing Interest

The authors declare that they have no known competing financial interests or personal relationships that could have appeared to influence the work reported in this paper.

Acknowledgements

This work has been performed within the framework of the international MUZIC (Mechanistic Understanding of Zirconium Corrosion) program. The authors gratefully acknowledge the industrial support from Westinghouse Electric (Sweden). This research was supported by

an Australian Government Research Training Program (RTP) Scholarship. This work was undertaken with the assistance of resources and services from the National Computational Infrastructure (NCI), which is supported by the Australian Government; the Multi-modal Australian Sciences Imaging and Visualisation Environment (MASSIVE); the Pawsey Supercomputing Centre, which is supported by the Australian Government and the Government of Western Australia; and was enabled by Intersect Australia Limited. Learn more at www.intersect.org.au.

Supplementary material

Supplementary material associated with this article can be found, in the online version, at doi:10.1016/j.scriptamat.2022.114652

References

- [1] A.T. Motta, L. Capolungo, L.Q. Chen, M.N. Cinbiz, M.R. Daymond, D.A. Koss, E. Lacroix, G. Pastore, P.C.A. Simon, M.R. Tonks, B.D. Wirth, M.A. Zikry, *J. Nucl. Mater.* 518 (2019) 440–460.
- [2] S. Suman, M.K. Khan, M. Pathak, R.N. Singh, J.K. Chakravarty, *Int. J. Hydrog. Energy* 40 (2015) 5976–5994.
- [3] A. Zieliński, S. Sobieszczuk, *Int. J. Hydrog. Energy* 36 (2011) 8619–8629.
- [4] Z. Tarzimgohadam, M. Rohwerder, S.V. Merzlikin, A. Bashir, L. Yedra, S. Eswara, D. Ponge, D. Raabe, *Acta Mater.* 109 (2016) 69–81.
- [5] G. McMahon, B.D. Miller, M.G. Burke, *npj Mater. Degrad.* 2 (2018) 2.
- [6] M.P. Brady, A.V. Ievlev, M. Fayek, D.N. Leonard, M.G. Frith, H.M. Meyer, A. J. Ramirez-Cuesta, L.L. Daemen, Y. Cheng, W. Guo, J.D. Poplawsky, O. S. Ovchinnikova, J. Thomson, L.M. Anovitz, G. Rother, D. Shin, G.-L. Song, B. Davis, *ACS Appl. Mater. Interf.* 9 (2017) 38125–38134.
- [7] O. Barrera, D. Bombac, Y. Chen, T.D. Daff, E. Galindo-Nava, P. Gong, D. Haley, R. Horton, I. Katzarov, J.R. Kermode, C. Liverani, M. Stophor, F. Sweeney, *J. Mater. Sci.* 53 (2018) 6251–6290.
- [8] H. Lambert, Y.S. Chen, *Philos. Trans. R. Soc. A* 375 (2017) 20170029.
- [9] S. Evers, C. Senöz, M. Rohwerder, *Sci. Tech. Adv. Mater.* 14 (2013).
- [10] G. Bertolino, G. Meyer, J.P. Ipia, *J. Alloys Compd.* 330–332 (2002) 408–413.
- [11] C. Vazquez, A.M. Fortis, P.B. Bozzano, *Proc. Mater. Sci.* 8 (2015) 478–485.
- [12] A. Couet, A.T. Motta, B. De Gabory, Z. Cai, *J. Nucl. Mater.* 452 (2014) 614–627.
- [13] Y.H. Jeong, K.O. Lee, H.G. Kim, *J. Nucl. Mater.* 302 (2002) 9–19.
- [14] Y.H. Jeong, H.G. Kim, D.J. Kim, B.K. Choi, J.H. Kim, *J. Nucl. Mater.* 323 (2003) 72–80.
- [15] H.G. Kim, S.Y. Park, M.H. Lee, Y.H. Jeong, S.D. Kim, *J. Nucl. Mater.* 373 (2008) 429–432.
- [16] M. Moorehead, Z. Yu, L. Borrel, J. Hu, Z. Cai, A. Couet, *Corr. Sci.* 155 (2019) 173–181.
- [17] A. Couet, A.T. Motta, R.J. Comstock, *ASTM, Zirconium in the Nuclear Industry: 17th International Symposium STP 1543*, 2015, pp. 479–514.
- [18] J. Hawes, P. Warnicke, P. Burr, D.F. Sanchez, D. Grolimund, J. Partezana, Y.-L. Chiu, S. Abolhassani, *Corr. Sci.* 190 (2021) 109630.
- [19] N. Ramasubramanian, P. Billot, S. Yagnik, *ASTM, Zirconium in the Nuclear Industry: Thirteenth International Symposium, 2002*, pp. 222–242.
- [20] K.N. Choo, S.I. Pyun, Y.S. Kim, *J. Nucl. Mater.* 226 (1995) 9–14.
- [21] J.P. Abriata, J.C. Bolcich, *Bull. Alloy Phase Diagr.* 3 (1982) 34–44.
- [22] J.Y. Park, B.K. Choi, Y.H. Jeong, Y.H. Jung, *J. Nucl. Mater.* 340 (2005) 237–246.
- [23] S. Banerjee, S.J. Vijayakar, R. Krishnan, *J. Nucl. Mater.* 62 (1976) 229–239.
- [24] G. He, J. Liu, K. Li, J. Hu, A.H. Mir, S. Lozano-Perez, C. Grovenor, *J. Nucl. Mater.* 526 (2019) 151738.
- [25] S. Doriot, B. Verhaeghe, J.L. Béchade, D. Menut, D. Gilbon, J.P. Mardon, J. M. Cloué, A. Miquet, L. Legras, *ASTM, Zirconium in the Nuclear Industry: 17th International Symposium STP 1543*, 2015, pp. 759–799.
- [26] B.D. Warr, M.B. Elmoselhi, S.B. Newcomb, N.S. McIntyre, A.M. Brennenstuhl, P. C. Lichtenberger, *ASTM, Zirconium in the Nuclear Industry: Ninth International Symposium 1132*, 1991, p. 740.
- [27] A. Perovic, V. Perovic, G.G. Weatherly, G.R. Purdy, R.G. Fleck, *J. Nucl. Mater.* 199 (1993) 102–111.
- [28] M. Ito, K. Ko, H. Muta, M. Uno, S. Yamanaka, *J. Alloys Compd.* 446–447 (2007) 451–454.
- [29] D. Khatamian, *J. Alloys Compd.* 293 (1999) 893–899.
- [30] D. Khatamian, *J. Alloys Compd.* 356–357 (2003) 22–26.
- [31] B.A. Cheadle, S.A. Aldridge, *J. Nucl. Mater.* 47 (1973) 255–258.
- [32] J. Liu, G. He, A. Callow, K. Li, K.L. Moore, H. Nordin, M. Moody, S. Lozano-Perez, C.R. Grovenor, *Acta Mater.* 215 (2021) 117042.
- [33] C.E. Coleman, R.W. Gilbert, G.J.C. Carpenter, G.C. Weatherly, *Phase Stability During Irradiation*, in: J.R. Holland, L.K. Mansur, D.I. Potter (Eds.), *The Metallurgical Society of AIME*, New York, 1981, p. 587.
- [34] Z. Yu, C. Zhang, P.M. Voyles, L. He, X. Liu, K. Nygren, A. Couet, *Acta Mater.* 178 (2019) 228–240.
- [35] G.K. Dey, R.N. Singh, R. Tewari, D. Srivastava, S. Banerjee, *J. Nucl. Mater.* 224 (1995) 146–157.
- [36] N.A.K. Kumar, J.A. Szpunar, *Mater. Sci. Eng. A* 528 (2011) 6366–6374.
- [37] S. Neogy, D. Srivastava, R. Tewari, R.N. Singh, G.K. Dey, S. Banerjee, *J. Nucl. Mater.* 322 (2003) 195–203.

- [38] A.V. De Walle, P. Tiwary, M. De Jong, D.L. Olmsted, M. Asta, A. Dick, D. Shin, Y. Wang, L.Q. Chen, Z.K. Liu, *Calphad* 42 (2013) 13–18.
- [39] G. Kresse, J. Furthmuller, *Comput. Mater. Sci.* 6 (1996) 15–50.
- [40] G. Kresse, J. Furthmuller, *Phys. Rev. B* 54 (1996) 11169–11186.
- [41] S.C. Lumley, S.T. Murphy, P.A. Burr, R.W. Grimes, P.R. Chard-Tuckey, M. R. Wenman, *J. Nucl. Mater.* 437 (2013) 122–129.
- [42] Y. Zhao, H. Li, Y. Huang, *J. Alloys Compd.* 862 (2021) 158029.
- [43] C. Jiang, C. Wolverton, J. Sofo, L.Q. Chen, Z.K. Liu, *Phys. Rev. B* 69 (2004) 1–10.
- [44] P.A. Burr, S.T. Murphy, S.C. Lumley, M.R. Wenman, R.W. Grimes, *J. Nucl. Mater.* 443 (2013) 502–506.
- [45] L.C. Liu, J.W. Wang, Y.H. He, H.R. Gong, *J. Membr. Sci.* 542 (2017) 24–30.
- [46] J. Qin, Z. Wang, D. Wang, F. Wang, X. Yan, Y. Zhong, C. Hu, H. Zhou, *J. Alloys Compd.* 805 (2019) 747–756.
- [47] F. Ren, W. Yin, Q. Yu, X. Jia, Z. Zhao, B. Wang, *J. Nucl. Mater.* 491 (2017) 206–212.
- [48] C. Jones, V. Tuli, Z. Shah, M. Gass, P.A. Burr, M. Preuss, K.L. Moore, *Sci. Rep.* 11 (2021) 4370.
- [49] B. Zhang, J. Su, M. Wang, Z. Liu, Z. Yang, M. Militzer, H. Chen, *Acta Mater.* 208 (2021) 116744.
- [50] A.J. Samin, D.A. Andersson, E.F. Holby, B.P. Uberuaga, *Phys. Rev. B* 99 (2019) 14110.
- [51] S.B. Gesari, M.E. Pronsato, A. Visintin, A. Juan, *J. Phys. Chem. C* 114 (2010) 16832–16836.
- [52] J. Radaković, K. Batalović, I. Maarević, J. Belošević-Čavor, *RSC Adv.* 4 (2014) 54769–54774.
- [53] A. Sadoc, E.H. Majzoub, V.T. Huett, K.F. Kelton, *J. Alloys Compd.* 356–357 (2003) 96–99.
- [54] Y.M. Dergachev, *Inorg. Mater.* 45 (2009) 863–866.
- [55] C. Elsasser, K. Ho, C.T. Chan, M. Fahnle, *J. Phys.* 4 (1992) 5207.
- [56] V. Shishov, M. Peregud, A. Nikulina, Y. Pimenov, G. Kobylansky, A. Novoselov, Z. Ostrovsky, A. Obukhov, *J. ASTM Int.* 2 (2005) 1–18.
- [57] J. Ribis, S. Doriot, F. Onimus, *J. Nucl. Mater.* 511 (2018) 18–29.
- [58] A.A. Turkin, A.V. Buts, A.S. Bakai, *J. Nucl. Mater.* 305 (2002) 134–152.
- [59] B.F. Kammenzind, B.M. Berquist, R. Bajaj, P.H. Kreyns, D.G. Franklin, *ASTM, Zirconium in the Nuclear Industry: Twelfth International Symposium, 2000*, pp. 196–233.
- [60] M. Griffiths, *J. Nucl. Mater.* 159 (1988) 190–218.
- [61] R. Gilbert, K. Farrell, C. Coleman, *J. Nucl. Mater.* 84 (1979) 137–148.
- [62] R.A. Holt, R.W. Gilbert, *J. Nucl. Mater.* 137 (1986) 185–189.
- [63] R. Adamson. Technical report, EPRI Technical Report 1013446, 2006.